

A Numerical Renormalization Solution for Self-Similar Cosmic Structure Formation

H. M. P. Couchman

Department of Physics and Astronomy, University of Western Ontario, London, ON, N6A 3K7

P. J. E. Peebles

Joseph Henry Laboratories, Princeton University, Princeton, NJ, 08544

ABSTRACT

We present results of a numerical renormalization approximation to the self-similar growth of clustering of a collisionless pressureless fluid out of a power-law spectrum of primeval Gaussian mass density fluctuations, $P(k) \propto k^n$, in an Einstein-de Sitter cosmological model. The self-similar position two-point correlation function, $\xi(r)$, seems to be well established. The renormalization solutions for $\xi(r)$ show a satisfying insensitivity to the parameters in the method, and at $n = -1$ and $n = 0$ are quite close to the Hamilton *et al.* formula for interpolation between the large-scale perturbative limit and stable small-scale clustering. The solutions are tested by the comparison of the mean relative peculiar velocity $\langle v_{ij} \rangle$ of particle pairs (ij) and the velocity derived from $\xi(r)$ under the assumption of self-similar evolution. Both the renormalization and a comparison conventional N-body solution are in reasonable agreement with the test, although the conventional approach does slightly better at large separations and the renormalization approach slightly better at small separations. Other comparisons of renormalization and conventional solutions are more demanding and the results much less satisfactory. Maps of the particle positions in redshift space in the renormalization solutions show more nearly empty voids and less prominent walls than do comparison conventional N-body solutions. The rms relative velocity dispersion is systematically smaller in the renormalization solution; the difference approaches a factor of two on small scales. There also are substantial differences in the frequency distributions of clump masses in renormalization and conventional solutions. The third moment S_3 from the distribution of mass within cells is in reasonable agreement with second-order perturbation theory on large scales, while on scales less than the clustering length S_3 is roughly consistent with hierarchical clustering but is heavily affected by shot noise.

Subject headings: cosmology: theory — cosmology: large-scale structure of universe — methods: numerical

1. Introduction

Clustering in a self-similar cosmogony is of interest because the simple physics might allow particularly accurate solutions. The reliability of a numerical approximation to a self-similar solution may be tested by the required scaling of properties with time and, in limiting cases, by comparison to analytic solutions. A reliable numerical self-similar solution in turn may be important as a benchmark for more realistic models for cosmic structure and as a guide to the formulation of analytic theories for self-similar evolution, as in the search for a closure *ansatz* for the BBGKY hierarchy (eg. Davis & Peebles 1977; Ruamsuwan & Fry 1992).

There can be aspects of a self-similar solution that are more accurately obtained by conventional methods than by the renormalization approach used here. An example is the mean relative proper peculiar velocity on large scales: we find the conventional solutions better fit the velocity derived from the two-point correlation function $\xi(r)$. Other discrepancies between renormalization and conventional solutions may be the fault of the conventional approach. An example found here is the frequency distribution of cluster masses on scales small compared to the clustering length. A different application of conventional methods might do better, of course, but until this can be established and the problem identified and remedied such discrepancies certainly indicate the need for caution in the application of numerical simulations.

There have been impressive advances in numerical N-body computations. For example, an early study of a self-similar solution used $N = 90$ particles (Peebles 1971); Peebles & Groth (1976) reached $N = 2000$; Aarseth, Gott, & Turner (1979), $N = 4000$; Efstathiou & Eastwood (1981), $N = 20,000$; and Efstathiou, Frenk, White, & Davis (1988), $N = 32^3$. More recent studies of numerical self-similar solutions use $N = 64^3$ (Colombi, Bouchet, & Hernquist 1996) and $N = 128^3$ (Jain, Mo, & White 1995; Yess & Shandarin 1996), and solutions with initial conditions that are not quite scale-invariant reach $N = 256^3$ (Thomas *et al.* 1997) and $N = 288^3$ (Jain & Bertschinger 1994). The requirements of a numerical self-similar solution are demanding, however. The clustering length r_o (at which the rms density contrast is close to unity) has to be much smaller than the size of the system. In a conventional solution the initial conditions are quite unrealistic on the scale of the interparticle separation, and this could compromise the clustering that develops on smaller comoving scales (Splinter *et al.* 1997). In a cube of unit width this would mean we want

$$N^{-1/3} \ll r_o \ll 1. \quad (1)$$

Even at $N = 256^3$ there is not much room to test that the clustering pattern has forgotten transients from the unrealistic initial conditions and has approached self-similar evolution.

A numerical renormalization scheme (Peebles 1985) offers a useful check on the possible effect of the limited range of the clustering length r_o in the conventional N-body approach. The renormalization method addresses the problem by a repeated rescaling that keeps r_o small compared to the size of the system. The first application of the method used only $N = 1000$ particles, and it certainly is timely to reconsider the approach with modern numerical techniques.

This study mainly uses $N = 64^3$ particles, and we compare the renormalization solution to a conventional computation with the same particle number.

In §2 we review the definition of the self-similar clustering problem. The great increase in the particle number allowed by present technology permits a more careful treatment of the large-scale density fluctuations introduced at each renormalization step. A new approach is presented in §3 along with a summary of the other steps in the renormalization method. Section 4 lists parameters for the computations. Solutions are obtained for two initial conditions, $n = -1$ and $n = 0$, in the primeval mass density fluctuation spectrum

$$P(k) \propto k^n. \quad (2)$$

The case $n = -1$ gives a not unreasonable first approximation to the galaxy distribution, although the relative velocity dispersion is too large because of the large mass density in the Einstein-de Sitter model. The case $n = 0$ offers a useful comparison. The numerical results presented in §5 are limited to a few commonly discussed statistics, including second-order moments in velocity and elements of third order in position.

2. Self-Similar Gravitational Clustering

Self-similar gravitational clustering in an expanding world model has no fixed characteristic length: the distribution and motion of the matter at world times t_1 and t_2 are statistically the same after lengths r_1 and r_2 at the two epochs t_1 and t_2 are scaled by the relation

$$r_2 = r_1(t_2/t_1)^\alpha. \quad (3)$$

The index α is a constant, and coordinate lengths r comove with the background cosmological model. The gravitational interaction of the matter is treated in the nonrelativistic Newtonian limit. This requires that peculiar velocities are much smaller than the velocity of light (and, which is almost equivalent, that the magnitude of the Newtonian potential of the departure of the mass distribution from homogeneity is much less than c^2), but otherwise allows arbitrarily strong nonlinear clustering. We use the Einstein-de Sitter model with negligible pressure, where the expansion parameter scales with proper world time as

$$a \propto t^{2/3}. \quad (4)$$

The power spectrum $P(k)$ of the mass distribution on scales large compared to the nonlinear clustering length is a power law (eq. [2]). If the clustering scale is growing in comoving units then this power law applies on any comoving length scale at small enough expansion parameter. In this sense equation (2) is the primeval mass fluctuation spectrum. The primeval fluctuations from homogeneity are assumed to be a random Gaussian process determined by the parameter n in $P(k)$.

Matter is treated as a pressureless collisionless fluid. In linear perturbation theory the density contrast of the mass distribution averaged over comoving scale r varies as

$$\delta\rho/\rho = \delta(\mathbf{r}, t) \propto t^{2/3} r^{-(3+n)/2}. \quad (5)$$

The crossing of orbits produces a coarse-grain average pressure, but this is the sum of noninteracting pressureless components with different velocities and mass densities. The effective Jeans length of the coarse-grain pressure must be on the order of the clustering length $r_o(t)$ defined by the mass autocorrelation function:

$$\xi(r) = \langle \rho(\mathbf{y}) \rho(\mathbf{r} + \mathbf{y}) \rangle / \langle \rho \rangle^2 - 1; \quad \xi(r_o) = 1. \quad (6)$$

This clustering length must scale with all others (eq. [3]):

$$r_o \propto t^\alpha \propto t^{4/(9+3n)} \propto a^{2/(3+n)}, \quad (7)$$

where the second expression follows from equation (5). The relation between the power spectrum index n and the length scaling index α is thus (Peebles 1965)

$$\alpha = 4/(9 + 3n). \quad (8)$$

If $n > -3$ the Fourier transform of $P(k)$, which is the mass autocorrelation function, is defined at large separation, and equation (8) indicates $\alpha > 0$, meaning the mass within the scale of nonlinear clustering increases with increasing time, as wanted. Equation (5) fails at $n > 4$, where the power spectrum on large scales is dominated by the coupling to small-scale nonlinear clustering (Peebles 1980, §28). Thus it is reasonable to seek solutions for the power law index in the range

$$-3 < n < 4. \quad (9)$$

Perhaps the most interesting generalization of the cosmological self-similar clustering problem would be to primeval density fluctuations that are scale-invariant but not Gaussian, that is, fractal.

There is increasing evidence that the mass density in matter capable of clustering is less than the Einstein-de Sitter value (Peebles 1997; Bahcall 1997). If the mass density is low the self-similar solution still may be useful as a description of conditions at large redshift, when the density parameter was close to unity, and as an initial condition for numerical integration to the present.

This discussion assumes that the self-similar solution exists and is unique, in the sense that Gaussian initial conditions with given power law index n evolve to a definite set of n -point correlation functions of the scaled lengths $x = r/t^\alpha$ and streaming velocities $v/t^{(\alpha-1/3)}$, and that the moments of the distributions of mass and momentum within cells are finite. We know of no evidence against this assumption but it seems prudent to bear the issue in mind.

3. The Numerical Renormalization Method

We summarize the elements of the numerical renormalization method, more details of which are in Peebles (1985), and then describe our new treatment of the primeval density fluctuations.

3.1. The Procedure

The model uses the motion of N particles in a cube with fixed comoving width and periodic boundary conditions, and iterates through the following steps. First, the equation of motion of the particles under their mutual gravitational interaction is integrated forward in time until the proper width of the cube has increased by the factor

$$a_f/a_i = 2^{(3+n)/2} = a_{\max}. \quad (10)$$

This increases the comoving clustering length r_o by a factor of two (eq. [7]). Second, to bring the ratio of the clustering length to the cube width back to the original value, adjoin eight copies of the particle positions and velocities to make a cube eight times the comoving volume of the original. Third, to scale all characteristic quantities back to the original values change units of length, time, and mass by the factors

$$r \rightarrow r/2, \quad a \rightarrow a/2^{(3+n)/2}, \quad t \rightarrow t/2^{(9+3n)/4}, \quad m \rightarrow m/8. \quad (11)$$

This scales proper peculiar velocities as $v \rightarrow v/2^{(1-n)/4}$. Fourth, fuse particles to bring the number back to the original value. This is accomplished by placing at random one in eight of the particles with its original mass and velocity at its place in each of the adjoined cubes. That is, with 50% probability each Cartesian position component of each particle is shifted by the width of the original cube. The Fourier modes on the scale of the box are depopulated by the renormalization. The final step is to repopulate these Fourier modes by shifting particle positions and velocities in a manner appropriate for the desired input spectrum. This step has been improved compared with the previous treatment, as discussed in §3.2.

The fourth step, the reduction from $8N$ to N particles by the selection of the position and scaled velocity of one particle, is statistically unbiased (Peebles 1985) but crude. It is not easily improved, however. It would be straightforward to identify neighboring groups of eight particles, and sensible to replace such a group with a single particle at the center of mass, but difficult to find a reasonable prescription for the velocity of the merged particle. The appropriate velocity would be that of the center of mass if the eight particles happened to be a gravitationally bound group. But if the group were selected from a small section of a virialized halo the center of mass velocity would be biased low and the selection of the scaled velocity of one of the particles in the group would keep the halo virialized. It would be simple and likely beneficial to replace the particle velocities in an unusually tight gravitationally bound pair (or group) with the center of mass velocity, just prior to the fourth step. This has not been done but might be considered in future applications of the renormalization method.

3.2. Application of Large-Scale Density Fluctuations

The operation described here applies mass density fluctuations on the scale of the renormalised cube so as to mimic the assumed primeval Gaussian random process.

We denote each Fourier component, or mode, in the periodic space defined by the cube by the comoving wavenumber $\mathbf{k} = 2\pi\mathbf{m}$, where \mathbf{m} is a triplet of integers which may be positive or negative. Thus the fundamental mode in the direction of the x -axis has $\mathbf{m} = (1, 0, 0)$. Let the mode amplitude immediately after a renormalization step be $\tilde{\delta}(\mathbf{k})$. In linear perturbation theory the integration of the equation of motion of the particles from $a_i = 1$ to $a_f = a_{\max}$ preserves the comoving wavenumber and brings the amplitude to $\tilde{\delta}(\mathbf{k})a_{\max}$. The next renormalization doubles the wavenumber of this mode, whilst leaving the amplitude unchanged (apart from the introduction of Poisson noise). Further iterations map the mode to wavenumbers $2^j\mathbf{k}$ with amplitude $\propto a_{\max}^j$.

We choose the set of modes, \mathbf{k}_j , $j = 1, \dots, l$, to be added to the cube after each renormalization step so that no new mode corresponds to one populated by the mapping $\mathbf{k} \rightarrow 2\mathbf{k}$ from any previous iteration. To achieve this it is sufficient to populate any mode for which $\prod(\mathbf{k}/2) = 0$, where \prod is the three-dimensional comb such that $\prod(\mathbf{k}) = 1$ if $\mathbf{k}/(2\pi)$ is an integer triple and vanishes otherwise. The added modes have amplitude $A(\mathbf{k}) \propto k^{n/2}$ and randomly chosen phases. In linear perturbation theory, after a series of J iterations the spectrum of modes has the form

$$\tilde{\delta}(\mathbf{k}) = \sum_{j=0}^{J-1} A(\mathbf{k}/2^j) e^{i\phi_{\mathbf{k}}} a_{\max}^j \prod(\mathbf{k}/2^j), \quad (12)$$

where $\phi_{\mathbf{k}}$ is a uniform random variate in $[0, 2\pi]$, and the phases are constrained such that $\tilde{\delta}(-\mathbf{k}) = \tilde{\delta}^*(\mathbf{k})$ to ensure a real density displacement. Equation (12) corresponds to the sum over a series of waves with decreasing density in wavenumber space and correspondingly increasing values of the amplitudes, $\propto a_{\max}^j$.

Our choice for the distribution of applied modes is

$$A(\mathbf{k}) = \begin{cases} \beta k^{n/2} (1 - \prod(\mathbf{k}/2)), & 1 \leq \left(\frac{k}{2\pi}\right)^2 \leq \left(\frac{k_c}{2\pi}\right)^2 = 22, \\ 0, & \text{otherwise.} \end{cases} \quad (13)$$

where β is a normalization constant. This adds 202 new (independent) modes at each iteration. The minimum-wavelength applied modes have $\mathbf{m} = (3, 3, 2)$ and the allowed permutations of this triplet. This corresponds to a wavelength of 0.21 of the box width. The choice of k_c is meant to satisfy two conditions: that we add modes only at relatively large scales, where the mass density fluctuations are close to linear, and that we populate a large number of modes so that the input fluctuations are not dominated by a small number of modes. In the treatment of Peebles (1985) modes, \mathbf{m} , were added with $m_{x,y,z} \in (-1, 0, 1)$ and $\mathbf{m} \neq 0$. With the requirement that the Fourier modes be Hermitian this corresponds to 13 new independent waves added at each renormalization.

The applied density fluctuations are close to Gaussian because they are the sum of a significant number of independent plane waves. There are unrealistic gaps in the spectrum, however; this is illustrated in Figure 1, which shows the wave numbers and amplitudes $|\delta_{\mathbf{k}}|$ for $n = -1$ applied at each iteration, and evolved forward in time in linear perturbation theory as described by equations (12) and (13). The scatter plot of the Fourier amplitudes of the mass distribution after the integration step of a stable renormalization solution shows traces of the bands in Figure 1, along with the dense distribution of points at high wavenumber resulting from nonlinear evolution. The spread in Fourier mode amplitudes resembles that seen in the conventional solution.

One can also renormalize after expansion by an integer amount, L , greater than 2. In this case the discussion proceeds exactly as above but with $a_{\max} = L^{(3+n)/2}$, while all terms containing $\prod(\mathbf{k}/2^n)$ become $\prod(\mathbf{k}/L^n)$.

The normalization of the mass-fluctuation power spectrum may be represented by the variance of the mass in a randomly placed sphere of radius R ,

$$\sigma^2(R) = \sum_{\mathbf{k}} |\tilde{\delta}(\mathbf{k})|^2 \tilde{W}^2(kR), \quad (14)$$

where $\tilde{W}(r)$ is the Fourier transform of a spherical top-hat window. Since a particular value of \mathbf{k} appears in only one of the iterations of the sum over j in equation (12), we can write equation (14) as

$$\sigma^2(R) = \sum_{j=0}^{J-1} a_{\max}^{2j} \sigma_0^2(L^j R), \quad (15)$$

where

$$\sigma_0^2(R) = \sum_{\mathbf{k}} A^2(\mathbf{k}) \prod(\mathbf{k}) \tilde{W}^2(kR) \quad (16)$$

is the mass variance input each new iteration. We may approximate the sum over \mathbf{k} in equation (16) as an integral in the usual way (with the restriction that $n > -3$). The discreteness effects here will be more important than is usual in making such an approximation. This is because of the small number of waves, the fact that the upper k cut at k_c does not translate into a smooth upper limit to $|\mathbf{k}|$, and the inclusion of the roughly 1/8 of waves per unit volume of k space which are missing in A in equation (13) because of the factor $1 - \prod(\mathbf{k}/2)$. Assuming that the top-hat filter $\tilde{W}(kR)$ approximates a sharp cutoff at $k = 1/R$, we find

$$\sigma_0^2(R) \propto [\min(1/R, k_c)]^{n+3} \quad \text{for } R \lesssim 1, \quad 0 \text{ otherwise;} \quad (17)$$

and hence

$$\sigma^2(R) \propto R^{-(n+3)} \left(\lceil \log_L(k_c/2\pi) \rceil + (a_{\max}^2 - 1)^{-1} \right). \quad (18)$$

Equation (18) is valid for $L^{-J} < R \lesssim 1/k_c$. For larger R there is a slow logarithmic departure from $R^{-(n+3)}$. The first term represents the waves from renormalizations which have some wavelengths of size comparable to the sphere size, the second the cumulative effect of waves from renormalizations which are much larger than the sphere size.

4. Parameters in the Numerical Solutions

Units for the renormalization computation are chosen so the comoving width of the cube is $r = 1$, the initial value of the expansion parameter is $a = 1$, the gravitational constant is $G = 1$, and the particle mass is $m = 1/N$ for N particles in the cube. In these units the initial mean mass density is $\rho_i = 1$ and the initial time is $t_i = (6\pi)^{-1/2}$. The pairwise particle force is that of the interaction between “softened” particles with density profile $\rho \propto (1 - r/c)$ at $r \leq c$ and $\rho = 0$ at $r > c$, where c is an adjustable softening length. This is the standard “S2” particle shape of Hockney & Eastwood (1981). With this definition of c , the peak in the force law is at $0.78c$. The particle separation at the peak is close to that for a standard Plummer force, $r/(r^2 + c^2)^{3/2}$, which is at $c/\sqrt{2}$, but the transition between the linear form at $r \ll c$ and the inverse square form at $r \gg c$ is sharper than for the Plummer force. The softening, or “cutoff”, length c is held constant in comoving coordinates.

Inter-particle forces in the periodic simulation cube are computed using the AP³M technique (Couchman 1991) and particle positions and velocities are updated using time-centered leapfrog. The expansion following each renormalization, which corresponds to a time range from $t_i = (6\pi)^{-1/2}$ to $t_f = a_{\max}^{3/2} t_i$, is integrated in 400 equal time steps. The results obtained using half this number of time-steps are statistically indistinguishable from those presented below.

After each renormalization, new modes are added by shifting the particle velocities and positions in real space using the appropriate sinusoidal wave displacements. Since we are adding relatively few waves at each iteration (eq. [13]) this does not significantly increase the computational effort. The same method is used to generate initial conditions for the conventional simulations, but at considerably greater computational expense.

We define the normalization of the waves added at each iteration (set by β in eq. [13]) by $\sigma_0(R = 0)$ using equation (16), and we refer to this input parameter simply as σ_0 . This equals the rms fluctuation added at each iteration on scales much smaller than $2\pi/k_c$ (eq. [13]).

The convergence of the renormalization method is rapid, and typically after six iterations there is little scatter from iteration to iteration. To assure elimination of transients we evolve through at least ten iterations prior to saving the first realization. In the realizations, particle positions and velocities are saved at the end of the integration step (immediately before renormalization), at every fifth iteration, to accumulate five realizations. The five iterations through the renormalization loop between saved realizations serve to suppress correlations among realizations. Error flags shown in the next section are the full spread of values from the five realizations. In the numerical results the length unit for particle separations r is the width of the cube, and particle velocities use the proper length ra_{\max} and the proper time unit for the computation, where the expansion time is $a_{\max}^{3/2}(6\pi)^{-1/6}$.

We choose for our standard renormalization solution the parameters

$$n = -1, \quad N = 64^3, \quad c = 0.001, \quad \sigma_0 = 0.1. \quad (19)$$

The power law index n gives a reasonably close fit to the shape of the galaxy two-point correlation function.

The comparison solution, from a conventional N-body computation, uses the first three parameters in equation (19). In an effort to make the comparison and standard renormalization solutions as comparable as possible, in one of the conventional realizations we use the phases of the Fourier components that were applied at each renormalization step for the corresponding set of wavenumbers. In the conventional simulation, with 64^3 particles, wavemodes up to 32 times the fundamental in the cube are used in the initial conditions. Matching phases from the renormalization computation involves saving the phases from the last 6 iterations (since $2^{6-1} = 32$) of the standard run. New random phases are introduced for the Fourier components that were not applied in any of these renormalization steps. The result is that one can see some similarity of features in maps of particle positions in the renormalization and conventional realizations. This is seen in Figure 2, which compares maps of particle positions in a renormalization realization and in a “phase-matched” conventional realization. The statistical results in §4 are averages across this “phase-matched” conventional realization and four other conventional realizations initialized with independently chosen random phases.

The initial density fluctuations in the conventional simulation are applied by the distortion of a distribution of particles initially at the vertices of a cubic lattice. The net expansion factor and the amplitude of the applied density fluctuations are set by the following considerations. In the numerical solution evolved from conventional initial conditions the mass variance in spheres arising from a linear input spectrum $|\delta(\mathbf{k})|^2 = \beta^2 k^n$ is $\sigma^2(R) \propto R^{-(n+3)}$, where the implied constant of proportionality is the same as that in equation (18). Thus we must increase the amplitude of the waves input to the conventional solution by a factor of $(\lceil \log_L(k_c/2\pi) \rceil + (a_{\max}^2 - 1)^{-1})^{1/2}$ which, for $L = 2$ and $k_c/2\pi = \sqrt{22}$, is a factor of approximately 1.8. Note, that there are several approximations involved in the derivation of equation (18) which weaken its predictive power and, furthermore, we cannot expect accurate matching of the two types of initial conditions over the full range of scales in the simulations. Enhancing the amplitude by the factor indicated nonetheless gives a good match between the final correlation amplitudes of the renormalized and conventional solutions.

In the standard renormalization solution the input fluctuation at each iteration is $\sigma_0 = 0.1$. After four further renormalisations these waves would dominate fluctuations on the scale of the mean interparticle spacing and contribute an rms fluctuation, in linear theory, amounting to $0.1 \times 2^4 = 1.6$. (We have ignored the contribution from waves input five renormalisations ago as these all now have wavenumbers at or beyond the Nyquist frequency.) The total rms fluctuation amplitude on this scale from all iterations would be of order 1.8 times greater (eq. [18]), giving a total linear rms fluctuation of roughly three. In order that all waves in the initial conditions for the conventional solution are in the linear regime we have started the conventional simulation with $a_i = 0.1$ with a corresponding decrease of a factor of ten in the input wave amplitudes. The rms fluctuations on the smallest scales at the start of the conventional simulation are thus of order

0.3. A test with an initial amplitude 5 times lower (with expansion starting at $a_i = 0.02$) yields results that are statistically indistinguishable.

The time interval corresponding to expansion from $a = 0.1$ to $a_{\max} = 2$ in the comparison solution is integrated using time-centred leapfrog, as before, with 918 equal steps. Each timestep in this case corresponds to 2/3 of that for the renormalization iterations. A shorter timestep ensures that the rapid expansion at the start of the conventional simulation is accurately followed. A test with twice as many timesteps gives the same statistical results.

At relatively large separations we get good statistical reliability of the estimates of the two-point position correlation function and the one- and two-point velocity statistics by using a random sample of a fraction $f = 0.1$ of the particles. At separations $r < 0.05$ the statistics are based on all particle pairs except where otherwise noted.

4.1. Results

In the maps in Figure 2 the length scale has been adjusted so that the clustering length r_o agrees with the galaxy clustering length, and the selection function is a rough approximation to that of the Las Campanas redshift survey (Schechter *et al.* 1996; Lin *et al.* 1996). Parts (a) and (b) show a slice in the standard renormalization solution, and parts (c) and (d) show the same slice in the comparison conventional solution in which wavenumbers in common with those applied at the renormalization steps have the same phases (the “phase-matched” pair). In (a) and (c) the radial variable is the distance, and in (b) and (d) it is the redshift. Because many of the phases of Fourier components for low wavenumbers are the same one can see similarities in the clustering pattern in the renormalization and conventional realizations.

In Figure 2 and other maps of the particle distributions the low density regions between the prominent mass concentrations are more nearly empty in the renormalization case. In maps of all particle positions in thin parallel slices one can see in the low density regions remnants of the perturbed lattice in the initial conditions for the conventional solution. They do not appear in the renormalization solution, of course. The “walls” in the redshift maps are less prominent in the renormalization solution. This may be a result of the stronger small-scale clustering and weaker large-scale motions in the renormalization solution. On scales $\gtrsim r_o$ infall velocities $|v(r)|$, as measured by the mean pairwise velocity, are systematically lower in the renormalization solution. This will tend to de-emphasize the sharpness of walls in redshift-space in the renormalization solution. The fractional difference of $|v(r)|$ in renormalization and conventional solutions is about 10% at the correlation length (0.013 times the box width) rising to 20% at 0.1 times the box width. The differences thus are not large but perhaps contribute to the difference in appearance of the maps.

Figure 3 shows how parameter changes affect the two-point position correlation function $\xi(r)$ in the renormalization solution. The correlation functions are based on a sampling fraction

of 0.1 of the particles, and the error bars are the maximum scatter across five realizations. The correlation function is defined by the usual relation, $1 + \xi = N_p/(n\delta V)$, where N_p is the mean number of neighbors of a particle in the distance range of the spherical shell with volume δV , and $n = N/V$ is the mean particle number density in the box. There is no edge correction because space is periodic. The total number of pairs is fixed, and the correlation function therefore satisfies the usual constraint, $\int d^3r \xi(r) = 0$ for $N \gg 1$, where the integral is over the box volume.

The standard renormalization solution in Figure 3 is shown as triangles. In the solution plotted as asterisks the amplitude of the applied density fluctuations is a factor of three larger than in the standard solution. In a self-similar solution this is equivalent to adjusting the length scale by the factor $r \rightarrow 3^{2/(3+n)}r$ (eq. [5]). Since $n = -1$, the particle separations in Figure 3 have been scaled by a factor of three. The gravitational interaction cutoff length in this solution is $c = 0.003$, so this length appears in the plot at separation 0.001, at the right-hand arrow. The ratio of clustering length r_o to inverse square cutoff length, c , thus is the same in the standard solution (triangles) and this solution plotted as asterisks. The difference between these solutions at one third the cutoff length is an indication of sensitivity to parameters in the renormalization method. The close agreement at larger separations is a significant indication that we have a good approximation to the self-similar solution. In the solution plotted as squares the applied amplitude is three times the standard solution and the cutoff length, c , is the same so c appears in Figure 3 at separation 0.00033, at the left-hand arrow. This solution also is in satisfactory agreement with the standard one. Finally, the circles show a solution with particle number three times the standard case. As in the other solutions the correlation function is the average across five realizations each separated by five renormalization steps. We see that changing N has very little effect on the two-point correlation function.

Efstathiou and Eastwood (1981) introduced another useful test of self-similarity, based on the relation between the two-point position correlation function $\xi(r)$ and the mean relative peculiar velocity $v(r)$ of particle pairs at separation r ,

$$\frac{\partial \xi}{\partial t} = -\frac{1}{r^2 a} \frac{\partial}{\partial r} r^2 (1 + \xi) v(r) = -\alpha \frac{r}{t} \frac{\partial \xi}{\partial r}. \quad (20)$$

The first part expresses conservation of particle pairs. The second part follows from the scaling relation in equations (3) and (8). In a self-similar solution $v(r)$ derived from $\xi(r)$ using the second part of equation (20) agrees with the mean relative peculiar velocity of particle pairs at separation r . The second part of equation (20), after multiplication by r^2 and integration over r (by parts on the right hand side), gives

$$v(r) = \frac{\alpha a}{t} \frac{r}{1 + \xi(r)} \left\{ \xi(r) - \int_V \xi dV/V \right\}, \quad (21)$$

where V is the volume of a sphere of radius r . This is a convenient form with which to test for self-similar behavior: ξ is measured in the straightforward manner described above, whilst $\int_V \xi dV$ is obtained directly from the mean count of neighbors within distance r of a particle.

In the bottom panels in Figures 4 to 6 the solid line is the result of predicting $v(r)$ from the measured $\xi(r)$ using equation (21). The open circles in the lower panels are the means $\langle v_{ij} \rangle$ of the relative peculiar velocities of particle pairs (ij) , and the error flags are the scatter of the means across the five realizations, in both renormalization and conventional solutions. The error flags for the $\langle v_{ij} \rangle$ at the smallest separations plotted are larger in the conventional solution because the rms scatter in relative velocities of particles is larger and the number of pairs is smaller.

In the standard renormalization solution shown in Figure 4 the mean relative velocities of particle pairs is quite close to what is expected in a self-similar solution at separations smaller than about $2r_o$, while at larger separations there is a significant systematic difference. The same is true of the renormalization solution for $n = 0$ in Figure 5. This difference between $\langle v_{ij} \rangle$ and $v(r)$ at large r might be a result of the disturbance of the system by renormalization at every factor $2^{(3+n)/2}$ expansion, and we might expect that this disturbance is largely forgotten on smaller scales, consistent with the success of the scaling test. The discrepancy goes the other way in the conventional solution in Figure 6, again as one might have anticipated: the solution is a good approximation on mildly nonlinear scales but does less well in the deeply nonlinear sector where there may be incomplete suppression of transients from the initial conditions. In the conventional numerical self-similar solution (from S. White) used by Jain (1997), with particle number $N = 100^3$ and power law index $n = -1$, the departure from self-similar behavior is less significant than in our conventional solution in Figure 6 although the error bars are significantly bigger in Jain’s Figure 2.

The solid lines in the upper panels of Figures 4 to 6 are the power law,

$$\xi \propto r^{-\gamma(n)}, \quad \gamma(n) = (9 + 3n)/(5 + n). \quad (22)$$

This applies in the self-similar solution when the time scale for the evolution of the mean clustering (measured in physical length units) is much longer than the Hubble time. In this case the mean relative peculiar velocity is the negative of the Hubble relation, which is shown in the dashed curve in the lower panels of the figures. All solutions here and in Jain (1997) agree that there is significant infall in physical length units at separations comparable to the clustering length r_o . This infall makes the logarithmic slope of $\xi(r)$ steeper than $\gamma(n)$. In the standard solution with $n = -1$ the result is not far from the power law shape of the galaxy two-point correlation function. The departure from a power law is more prominent in Jain’s (1997) solution, perhaps because the larger particle number allows the solution to reach larger values of ξ . At $n = 0$ the slope of $\xi(r)$ in our solution is steeper than the galaxy function at $r \sim r_o$, and the departure from a power law more prominent.

Figures 7 and 8 compare the two-point correlation functions in the numerical solutions to the method of Hamilton *et al.* (1991) for interpolation between equation (22) on small scales and linear perturbation theory on large scales. The dashed curves are the fitting function for the Hamilton *et al.* method from Peacock & Dodds (1996), and the solid curves are the fitting function of Jain, Mo, & White (1995). The feature in the latter at $r \sim r_o$ is much less prominent

in the integral $\int_0^r r^2 \xi(r) dr$ considered by Jain *et al.*, but the Peacock & Dodds form does better fit our renormalization solutions. This feature aside, there is very close consistency with the renormalization solutions at $n = -1$ and $n = 0$ and with the conventional solutions for correlation amplitudes around unity.

It might be mentioned that the Hamilton *et al.* method assumes statistically stable small-scale clustering, as reflected in equation (22). Stability is difficult to demonstrate on theoretical or numerical grounds (Ruamsuwan & Fry 1992; Jain 1997); the striking success of the interpolation method offers some support for stability.

Figure 9 shows second moments of the relative peculiar velocities of particle pairs as a function of their separation, in the standard renormalization and conventional solutions with $n = -1$. The rms dispersion σ_r in the component along the line connecting the particles is computed relative to the mean value $\langle v_{ij} \rangle$. The transverse component σ_t is normalized to one direction orthogonal to the line connecting the particle pair, so $\sigma_r = \sigma_t$ if the velocities are isotropic relative to the mean. The renormalization and conventional solutions agree that σ_r is systematically greater than σ_t at $r > c$. The velocity dispersion is distinctly larger in the conventional solution, and the difference grows with decreasing separation to a factor of two at the smallest separation plotted (which is well within the force cutoff length c). If the mass autocorrelation function at small scales varied as $\xi \propto r^{-\gamma}$, and the clustering on average were not evolving (in physical units), the relative velocity dispersion would vary as $\sigma \propto r^{1-\gamma/2}$. There is not enough range between c and r_o for a test, but the renormalization solution does show the expected slow increase of the relative velocity dispersion with increasing separation of the particles at $r \lesssim r_o$.

Figure 10 shows distributions of the absolute values of one Cartesian component of the relative proper velocity of particle pairs. We compare the “phase-matched” pair of conventional and renormalization realizations; the distributions from the other four members of each of the ensembles for $n = -1$ have the same main features. Consistent with Figure 9, the renormalization solution has a much narrower distribution at small separation and a perceptibly narrower distribution at relatively large separation.

Figure 11 shows distributions of the counts of neighboring particles within given distances of a particle. The abscissa is the count n of neighbors. The ordinate is the fraction of particles that have n or more neighbors within the given distance. The histograms for the renormalization realizations are plotted as solid lines and for the conventional realizations as dotted lines. The “phase-matched” pair are the heavy solid and dotted lines. If the richest concentration within scale r contained n_x particles, and the next richest concentration on this scale contained distinctly fewer, it would produce a shoulder or near level section at probability $\sim n_x/64^3$ for $\sim n_x$ neighbors. A prominent example is in the “phase-matched” conventional realization at $r = 0.005$. As it happens, at this radius the distributions in the “phase-matched” pair are at the extreme high and low sides of the realizations even though this pair was designed to have similar space distributions. There are too few realizations to decide whether the shoulder effect is more common

in the renormalization or conventional approach.

Despite the scatter among realizations there is a clear trend in Figure 11: the renormalization solution tends to have less extreme mass concentrations at $r \gtrsim 0.005$ and larger concentrations on smaller scales. At $r \lesssim 0.002$ the difference is seen in the second moment (Fig. [7]), but at larger separations it has little effect on $\xi(r)$ or on the third moment, as discussed next. The rms scatter in the relative gravitational acceleration of particle pairs depends on the fourth moment, and the differences in distributions of neighbours likely accounts for the systematic difference in relative velocity dispersions. At large separations the smaller velocity dispersion in the renormalization solution would be expected from the less common occurrence of strong mass concentrations. At small separations the more numerous close pairs in the renormalization solution likely are in a clustering hierarchy that extends to smaller scales, whereas close pairs in the conventional solution are more likely to be accidentals moving with larger relative velocities in larger clumps.

Figure 12 shows a commonly applied measure of the skewness of the mass distribution in randomly placed cells. Because there is some potential for confusion we remind the reader of the following results. A stationary and isotropic random point process with mean particle number density n may be characterized by its N -point correlation functions. The second and third are defined by the joint probabilities of finding particles in two and three disjoint volume elements:

$$dP_{12} = n^2[1 + \xi(12)]dV_1dV_2, \quad (23)$$

$$dP_{123} = n^3[1 + \xi(12) + \xi(23) + \xi(31) + \zeta(123)]dV_1dV_2dV_3. \quad (24)$$

The argument of the two-point function is the distance between the two volume elements. The arguments of the three-point function are the three sides of the triangle defined by the three volume elements. The mass in a randomly placed sphere of radius r and volume V is $M = mN$, where m is the particle mass. The expectation value is $\bar{M} = m\bar{N}$, where $\bar{N} = nV$. The mass density contrast in the sphere is

$$\delta = M/\bar{M} - 1. \quad (25)$$

The ratio of the third central moment to the square of the second central moment of the probability distribution in the mass contrast is

$$\begin{aligned} S_3 &= \frac{\langle \delta^3 \rangle}{\langle \delta^2 \rangle^2} = \frac{\bar{N} \langle (N - \bar{N})^3 \rangle}{[\langle (N - \bar{N})^2 \rangle]^2} \\ &= \frac{\int \zeta(123) d^3V/V^3 + 3\bar{N}^{-1} \int \xi(12) d^2V/V^2 + \bar{N}^{-2}}{[\int \xi(12) d^2V/V^2 + \bar{N}^{-1}]^2}. \end{aligned} \quad (26)$$

The integrals are over the sphere volume V . If the points were tracers of the distribution of an underlying continuous fluid with mass density $\rho(\mathbf{r})$, such that a point is placed in the volume element dV at position \mathbf{r} with probability

$$dP \propto \rho(\mathbf{r})dV, \quad (27)$$

then the shot or discreteness noise terms in equation (26) would be a consequence of the limited sampling of the mass distribution. In this case the shot noise terms should be removed. This is done in the expression

$$S'_3 = \frac{\int \zeta(123) d^3V/V^3}{[\int \xi(12) d^2V/V^2]^2} = \frac{\bar{N}[\langle(N - \bar{N})^3\rangle - 3\langle(N - \bar{N})^2\rangle + 2\bar{N}]}{[\langle(N - \bar{N})^2\rangle - \bar{N}]^2}. \quad (28)$$

One can define mass correlation functions by replacing each particle with a sphere of volume δV and internal density $m/\delta V$. In the limit $\delta V \rightarrow 0$ the mass two-point or autocorrelation function and the mass three-point function are

$$\begin{aligned} \xi_\rho(12) &= \xi(12) + \delta(12)/n, \\ \zeta_\rho(123) &= \zeta(123) + [\delta(12)\xi(23) + \delta(23)\xi(31) + \delta(31)\xi(12)]/n + \delta(12)\delta(23)/n^2, \end{aligned} \quad (29)$$

where the position correlation functions ξ and ζ are defined in equations (23) and (24). When ξ and ζ are replaced by ξ_ρ and ζ_ρ in the ratio of integrals in equation (28) the Dirac delta functions in equation (29) produce the extra terms in equation (26).

In numerical N-body solutions such as the ones used in this study the mass distribution actually is that of the particles, and therefore equation (26) (or the ratio of integrals in eq. [28] over the mass functions in eq. [29]) is the ratio of moments of the mass distribution that figures in the dynamics. The difference between equations (26) and (28) (where ξ and ζ are the position correlation functions in eqs. [(23) and (24)]) is a useful measure of the relative contributions to S_3 by shot noise and the clustering of particles. In a good approximation to a self-similar solution the shot noise is subdominant, of course.

Another measure of the importance of shot noise is provided by the two ratios

$$\langle(N - \bar{N})^2\rangle/\bar{N}, \quad \langle(N - \bar{N})^3\rangle/[3\langle(N - \bar{N})^2\rangle]. \quad (30)$$

When n is sufficiently large (and the particle mass correspondingly small), as in a good self-similar solution, these ratios are much larger than unity and equations (26) and (28) are equivalent.

The statistics in Figure 12 are derived from the “phase-matched” pair of realizations for $n = -1$. The ratios in equation (30) are plotted as the dotted curves. They show that the shot noise contribution to the skewness and variance is reasonably small at cell radius r equal to the clustering length r_o , but shot noise is dominant in the $n = -1$ case at $r \lesssim 0.1r_o$. (The situation is a little better at $n = 0$ because $\xi(r)$ is larger.) This is our most vivid illustration of the limited dynamical range in length scale available for N-body simulations of the nonlinear sector of clustering solutions even when $N^{1/3}$, which sets the dynamical range, is within a factor of four of what is now feasible.

The solid lines in Figure 12 are the ratios S_3 of mass moments (eq. [26]) for $n = -1$. To illustrate the contribution of the shot noise terms to the mass moments we show as the dashed

lines S'_3 based on the reduced correlation functions (eq. [28]). Colombi, Bouchet, & Hernquist (1996) study S'_3 in their conventional self-similar solution. Their results are in reasonably close agreement with S'_3 from our conventional solution at $r \lesssim 0.001$, but they do not find the rapid increase in noise at smaller separation.

The comparison of solid and dashed lines in Figure 12 shows that the shot noise contribution to S_3 is appreciable but not dominant at $r = r_o$, and the shot noise contribution diverges at $r = 0.1r_o$. This agrees with the measures of shot noise in equation (30).

At large sphere radius shot noise is unimportant and second-order perturbation theory should apply. Here Bernardeau (1994a,b) finds

$$S_3 = 34/7 - (3 + n), \quad (31)$$

for Gaussian initial density fluctuations, and

$$S_3^{\text{Zel}} = 4 - (3 + n), \quad (32)$$

for the Zel'dovich approximation. Equation (31) is plotted as the horizontal dotted lines in Figure 12. The upturn in S_3 at $r \sim 0.1$ in the numerical solutions is of doubtful significance because the sphere radius approaches the box size. At $r_o \lesssim r \lesssim 0.1$ the conventional solution is somewhat closer to perturbation theory with Gaussian initial conditions, consistent with the somewhat better large-scale performance of the conventional solution in the scaling test in Figures 4 to 6. In the renormalization solution, density fluctuations are applied by the Zel'dovich approximation, and the lower skewness in equation (32) might be expected to persist through several iterations. This may contribute to the lower value of S_3 for the renormalization solution.

At $r \lesssim c = 0.001$ the correlation functions in the renormalization and conventional solutions are quite different (Fig. [7]). This difference in $\xi(r)$ is not reflected in S_3 , because the central mass moments are dominated by discreteness noise and the mass moments in S_3 consequently are at the shot noise limit.

At $c \lesssim r \lesssim r_o$ the skewness of the mass distribution can be compared to that of the galaxy distribution. Useful approximations to the galaxy correlation functions at $r \lesssim r_o$ are

$$\xi = (r_o/r)^\gamma, \quad \zeta = Q(\xi_{12}\xi_{23} + \xi_{23}\xi_{31} + \xi_{31}\xi_{12}), \quad (33)$$

where

$$\gamma = 1.8, \quad Q \simeq 1. \quad (34)$$

A Monte Carlo integration over the three-point function gives $S_3 = 3.1Q$ for $\gamma = 1.8$ and $S_3 = 3.0Q$ for $\gamma = 2$. A logarithmic slope $\gamma = -2$ is appropriate for the two-point correlation function of the $n = -1$ renormalization solution over the range of scales below r_o for which the measured S_3 is not completely dominated by shot noise ($10^{-3} \lesssim r \lesssim 10^{-2}$). The value of S_3 in the numerical solutions is in line with these numbers, although the comparison is not very sharply defined because of the

large shot noise component in the solutions. The comparison of the self-similar solution and the galaxy distribution is of limited significance in any case, of course, for if the expansion of the universe is scale-invariant (Einstein-de Sitter) galaxies do not trace mass and if galaxies are useful mass tracers the expansion is not scale-invariant.

5. Discussion

N-body approximations to self-similar clustering are severely limited by shot noise. In our standard solution for $n = -1$ there is only a factor of ten difference between the nonlinear clustering length r_o and the sphere radius at which shot noise dominates the mass moments (Fig. [12]). In this aspect our numerical solutions are quite unrealistic approximations to self-similar solutions at $r \lesssim 0.1r_o \sim 0.001 \sim c$. The parameters in equation (19) were chosen so that shot noise dominates roughly at the force law cutoff c .¹

In the numerical renormalization approach the value of r_o changes by a factor of two between iterations. The factor of ten range of scales between shot noise domination and nonlinear clustering at the end of the integration step accommodates this factor of two swing of r_o , but the situation is at best marginal. The small-scale behavior of the renormalization solution thus must be treated with caution. We expect that the small-scale properties of a conventional solution with the same parameters are even less secure because of the difficulty of establishing that the solution truly approaches self-similar behavior. Thus we suspect the pronounced difference of clustering properties in our renormalization and conventional solutions with $N = 64^3$ (Fig. [11]) is mainly the fault of the latter.

Relaxation is assured in the numerical renormalization method, but at the price of a much poorer treatment of initial conditions. The coarse population of initial Fourier components in the renormalization approach is shown in Figure 1. For this reason we are inclined to place greater trust in the properties of conventional numerical solutions on mildly nonlinear scales. Our interpretation is consistent with the mean relative velocity test for self-similar behavior (Figs. 4 and 6): the renormalization solution does better on scales less than the clustering length r_o and the conventional solution does better on larger scales.

Despite the shortcomings of the conventional and renormalization methods the self-similar two-point mass autocorrelation function seems to be quite accurately and reliably established at $\xi \lesssim 100$. This is indicated by the excellent consistency of the renormalization and conventional

¹This situation is not likely to be improved by increasing r_o . In our standard renormalization solution (with $r_o = 0.013$) the rms fluctuation in counts in spherical cells is $\delta N/N = 1$ for sphere diameter $2r = 0.04$. For the primeval mass fluctuation spectrum $P(k) \propto k^{-1}$ this would scale to rms fluctuation $\delta N/N = 0.1$ at diameter $2r = 0.4$, if the count were not fixed in the box that has roughly twice this width. If r_o were significantly increased the two-standard-deviation mass fluctuations on the scale of half the box width would be mildly nonlinear and seriously constrained by the fixed number of particles in the box.

solutions for $\xi(r)$. In particular, $\xi(r)$ in our renormalization solutions must be quite close to the conventional solutions used to find the fitting functions for the Hamilton *et al.* interpolation (Figs. 7 and 8). As we have noted, conventional and renormalization solutions are in overall good agreement with the relative velocity test for self-similar evolution. Additional checks of the renormalization solution are the amplitude scaling (Fig. 3) and the stability under change of the particle number N . Indeed, the original results at $N = 1000$ are not much different from what we find at $N = 3 \times 64^3$.

The relative velocity dispersion (Fig. 9) and the frequency distributions of relative velocities and cluster masses (Figs. 10 and 11) are more demanding, and the comparison of renormalization and conventional solutions is much less satisfactory than for $\xi(r)$. Also disturbing is the difference of appearance of the voids and walls in the renormalization and conventional maps of particle positions (Fig. 2).

The discrepancies between conventional and renormalization solutions suggest that the numerical N-body predictions are uncertain on issues that are observationally relevant and important for theoretical analyses of self-similar evolution. Our understanding of these issues would be improved by using larger particle number N . An increase from the value in most solutions presented here, $N = 64^3$, to $N = 128^3$ has already been done for the conventional N-body method. An ensemble of five renormalization solutions requires about seven times the computation for five conventional solutions, which is feasible with present technology at $N = 128^3$. With all other parameters unchanged this would increase the mean number of neighbors at given comoving distance by a factor of eight, increasing the ratio of clustering length to the radius at shot noise dominance by the factor $2^{3/(3-\gamma)} \sim 5$. In addition to the exploration of differences between conventional and renormalization solutions, the larger particle number might allow a preliminary exploration of two questions. First, does the clustering hierarchy in the mass distribution, as reflected in the hierarchy of N-point correlation functions (as in eq. [33]), persist to scales much smaller than the clustering length r_o ? An alternative is that merging produces monolithic massive halos with radii scaling with r_o , as assumed by Sheth & Jain (1997). Second, are the distributions of relative velocities and positions consistent with statistically stable clustering on small scales, as assumed in equation (22)? We hope to present results on these issues from the analyses of renormalization and conventional solutions with $N = 128^3$ in due course.

We are grateful to Roman Scoccimarro for discussions that substantially improved this paper. The work was supported in part at the University of Western Ontario by NSERC of Canada, and at Princeton University by the US National Science Foundation. HMPC thanks CITA for hospitality whilst this work was completed.

REFERENCES

- Aarseth, S. J., Gott, J. R., & Turner, E. L. 1979, *ApJ*, 228, 664
- Bahcall, N. A. 1997, in *Unsolved Problems in Astrophysics*, eds. J. N. Bahcall & J. P. Ostriker (Princeton, Princeton University Press), p. 61
- Bernardeau, F. 1994a, *A&A*, 291, 697
- Bernardeau, F. 1994b, *ApJ*, 433, 1
- Colombi, S., Bouchet, F. R., & Hernquist, L. 1996, *ApJ*, 465, 14
- Couchman, H. M. P., 1991, *ApJ*, 368, L23
- Davis, M. & Peebles, P. J. E. 1977, *ApJS*, 34, 425
- Efstathiou, G. & Eastwood, J. W. 1981, *MNRAS*, 194, 503
- Efstathiou, G., Frenk, C. S., White, S. D. M., & Davis, M. 1988, *MNRAS*, 235, 715
- Gelb, J. M. & Bertschinger, E. 1994, *ApJ*, 436, 467
- Hamilton, A. J. S., Kumar, P., Lu, E., & Matthews, A. 1991, *ApJ*, 374, L1
- Hockney, R. W. & Eastwood, J. W. 1981, *Computer Simulation Using Particles*, McGraw-Hill, New York
- Jain, B. 1997, *MNRAS*, 287, 687
- Jain, B. & Bertschinger, E. 1994, *ApJ*, 431, 495
- Jain, B., Mo, H. J. & White, S. D. M., 1995, *MNRAS*, 276, L25
- Lin, H., Kirshner, R. P., Shectman, S. A., Landy, S. D., Oemler, A., Tucker, D. L. & Schechter, P. L., 1996, *ApJ*, 464, 60
- Peacock, J.A. & Dodds, S. J., 1996, *MNRAS*, 280, 19
- Peebles, P. J. E. 1965, *ApJ*, 142, 1317
- Peebles, P. J. E. 1971, *A&A*, 11, 377
- Peebles, P. J. E. 1980, *The Large-Scale Structure of the Universe* (Princeton:Princeton University Press)
- Peebles, P. J. E. 1985, *ApJ*, 297, 350
- Peebles, P. J. E. 1997, in *Unsolved Problems in Astrophysics*, eds. J. N. Bahcall & J. P. Ostriker (Princeton, Princeton University Press), p. 1
- Peebles, P. J. E. & Groth, E. J. 1976, *Astron Ap*, 53, 131
- Ruamsuwan, L. & Fry, J. N. 1992, *ApJ*, 396, 416
- Shectman, S. A., Landy, S. D., Oemler, A., Tucker, D. L., Lin, H., Kirshner, R. P. & Schechter, P. L., 1996, *ApJ*, 470, 172
- Sheth, R. & Jain, B. 1997, *MNRAS*, 285, 231

- Splinter, R. J., Melott, A. L., Shandarin, S. F., & Suto, Y. 1997, preprint (astro-ph/9706099)
- Thomas, P. A., Colberg, J. M., Couchman, H. M. P., Efstathiou, G. P., Frenk, C. S., Jenkins, A. R., Nelson, A. H. Hutchings, R. M., Peacock, J. A., Pearce, F. R. & White, S. D. M. 1997, astro-ph/9707018
- Yess, C. & Shandarin, S. F. 1996, ApJ, 465, 2

Fig. 1.— Modulus of the applied Fourier components in the renormalization (circles) and conventional (crosses) methods (eqs. [12] and [13]) for $n = -1$. For the renormalization method we assume linear perturbation theory, so at each iteration wavenumbers of previously applied components are doubled and the amplitudes $|\delta_k|$ are multiplied by the factor $a_{\max} = 2^{(3+n)/2}$. Wavenumbers are plotted in units of the fundamental wavenumber in the box. The input amplitude corresponds to $\sigma_0 = 0.1$ (eq. [16]).

Fig. 2.— Particle position maps in real (top) and redshift (bottom) space in strips of width corresponding to 6 hrs of right ascension at declination 32° and depth 1.5° . The standard renormalization solution is on the left, and the comparison conventional solution on the right. The length scale has been adjusted to make the clustering length equal to $H_0 r_0 = 540 \text{ km s}^{-1}$, close to what is observed for galaxies. The fraction of particle positions plotted as a function of distance approximates the selection function of the Las Campanas redshift survey.

Fig. 3.— Test of sensitivity of the position two-point correlation function $\xi(r)$ to parameters in the renormalization computation. The standard renormalization solution is shown as triangles, and the separation r on the abscissa is plotted in the units of this solution (where the box width is $r = 1$). Asterisks show the result of increasing the amplitude δ of the applied perturbation and the cutoff length c of the gravitational interaction by factors of three. Because $n = -1$, we compensate for the larger amplitude by scaling lengths by a factor of three (eq. [5]). The cutoff length thus is plotted at separation 0.001, at the right-hand arrow, the same as the standard solution. In the solution shown as squares the amplitude also is a factor of three larger than standard, so lengths have been scaled by a factor of three, and the cutoff length $c = 0.001$ appears at the left-hand arrow. The circles show the effect of increasing the particle number by a factor of three. Here δ is the same as the standard solution so the separations are plotted at the coordinate values in the solution.

Fig. 4.— Scaling test for the standard renormalization solution ($n = -1$). The solid line in the upper panel is the power law with index $\gamma = (9 + 3n)/(5 + n)$ for statistically stable clustering, and the circles in the upper panel are the two-point position correlation function. The scatter across the five realizations is smaller than the circles except at the three largest separations in the plot. The arrow is the cutoff length c for the inverse square force law. The circles in the lower panel are means of the relative peculiar velocities of particle pairs, and the solid curve is the mean velocity derived from the scaling law for the two-point correlation function, $\xi = \xi(r/t^\alpha)$ (eq. [21]). The dashed curve in the lower panel is $v = -r\dot{a}/a$, the peculiar relative velocity for physically stable mean clustering.

Fig. 5.— Scaling test for the renormalization solution for $n = 0$, as in Fig. 4.

Fig. 6.— Scaling test for the conventional solution for $n = -1$, as in Fig. 4.

Fig. 7.— Comparison of the Hamilton *et al.* (1991) interpolation of the two-point function $\xi(r)$ and the renormalization and conventional solutions at $n = -1$. The dashed curve is the fitting function from Peacock & Dodds (1996), and the solid curve is that of Jain *et al.* (1996). The arrow

marks the force law cutoff length c .

Fig. 8.— Comparison of the two-point correlation function in the renormalization solution for $n = 0$ and the Hamilton *et al.* interpolation formula, as in Fig. 7.

Fig. 9.— Relative peculiar velocity dispersions for $n = -1$. The top panel is the standard renormalization solution, and the bottom is the comparison conventional solution. The circles are σ_r , the rms fluctuation around the mean of the radial component of the relative peculiar velocity of particle pairs. The triangles are the rms value σ_t of the relative velocity transverse to the line connecting the particles, and normalized to one component, so in a isotropic distribution $\sigma_t = \sigma_r$.

Fig. 10.— Frequency distributions in the absolute value of one Cartesian component of the relative proper velocity difference of particle pairs, in three bins of separation each of width $\delta r/r \sim 0.5$. The bold histogram is the standard renormalization solution, and the thinner histogram is the comparison conventional solution, for the “phase-matched” pair of realizations for $n = -1$.

Fig. 11.— Cumulative frequency distributions of the counts of neighboring particles in spheres centered on each of the $N = 64^3$ particles in the $n = -1$ realizations. Histograms are shown (from left to right) for six different sphere radii: $r = 0.0002, 0.0007, 0.002, 0.005, 0.02$ and 0.05 . For each radius the solid histograms are the counts in the renormalization realizations and the dotted histograms the counts in the conventional realizations. The “phase-matched” pair are plotted as the heavier solid and dotted lines. The cumulative number of neighbors in the abscissa is plotted at the left-hand edge of each bar in the histogram.

Fig. 12.— Measures of the third moments of the mass distribution, based on the distribution of counts of particles in randomly placed spheres for the $n = -1$ simulations. The number of spheres used ranged from 10^8 for $r \leq 2 \times 10^{-3}$ to 10^5 for $r \geq 3 \times 10^{-2}$. The upper panel is the standard renormalization solution, and the lower panel is the comparison conventional solution. The solid line is the dimensionless skewness ratio S_3 of the third central moment to the square of the variance of the mass distribution, as defined in equation (26). The dashed line illustrates the effect of removing the shot noise contributions to the mass moments, as in equation (28). At radii smaller than plotted for the dashed curves the fluctuations are off the scale of the graph. Another measure of the shot noise contribution is the set of ratios in equation (30). These ratios are plotted as the dotted curves that asymptote at unity for the second moment and $1/3$ for the third moment. The horizontal line is the perturbation theory prediction for S_3 (eq. [31]).

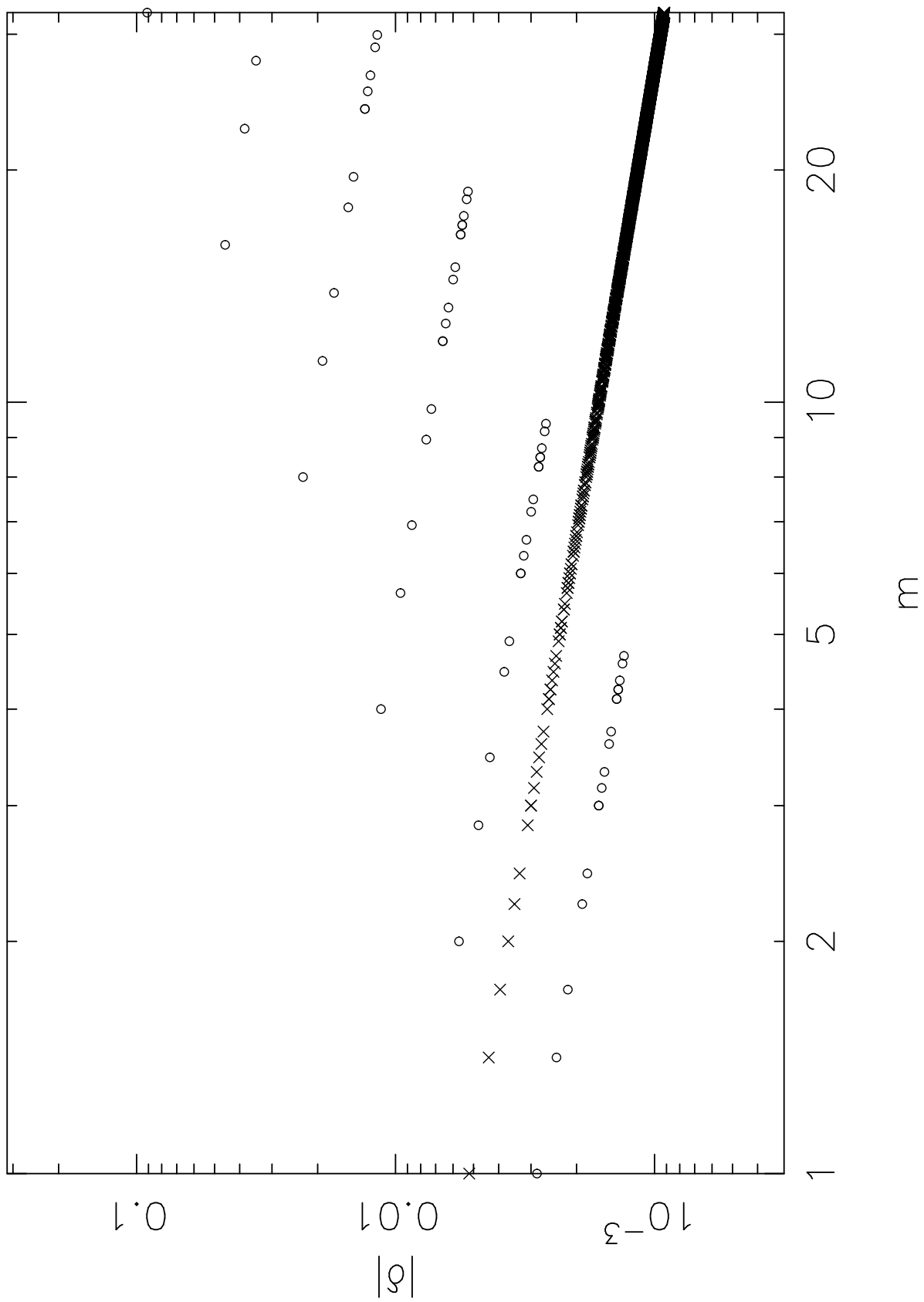


Fig. 1

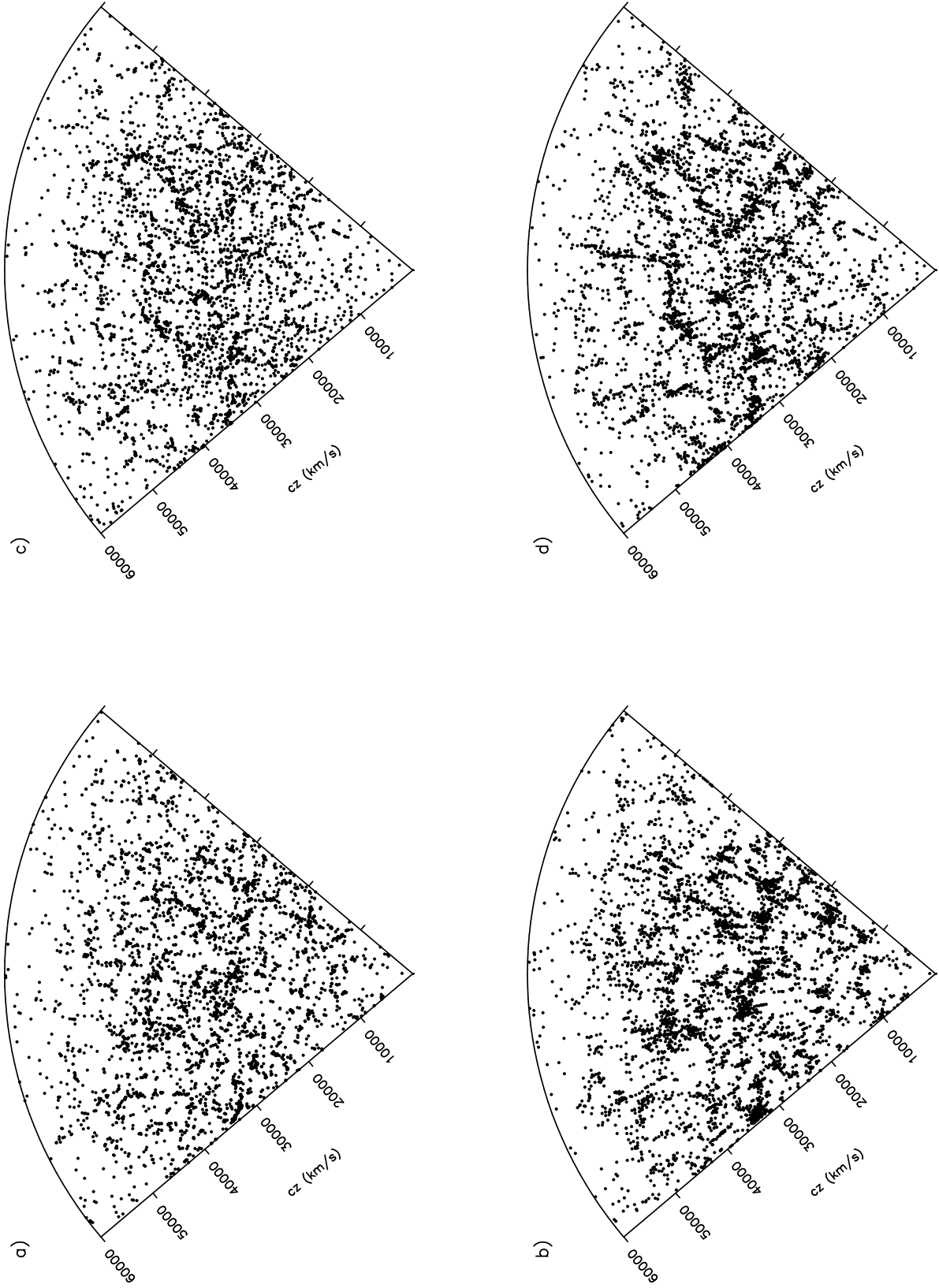


Fig. 2

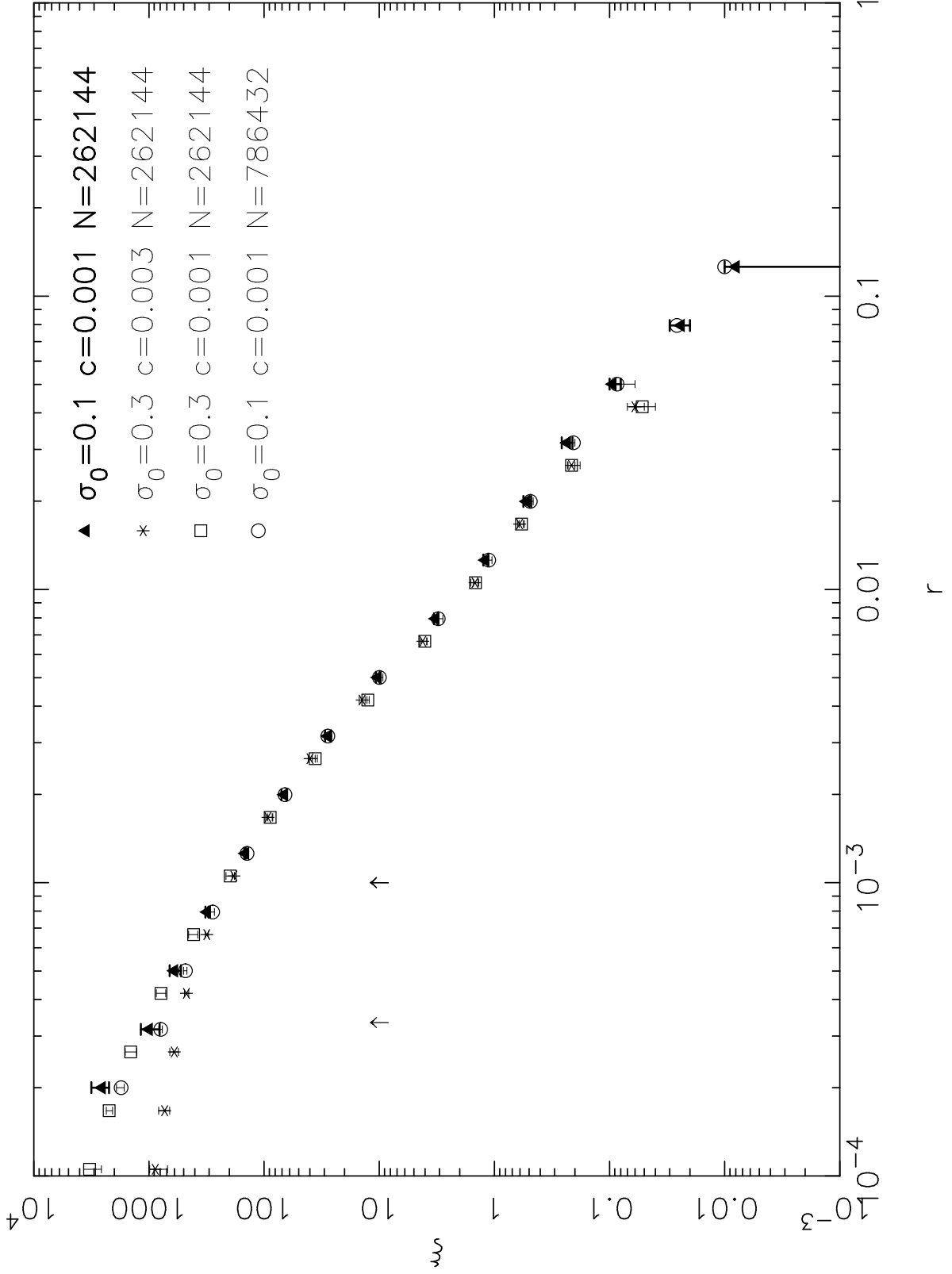


Fig. 3

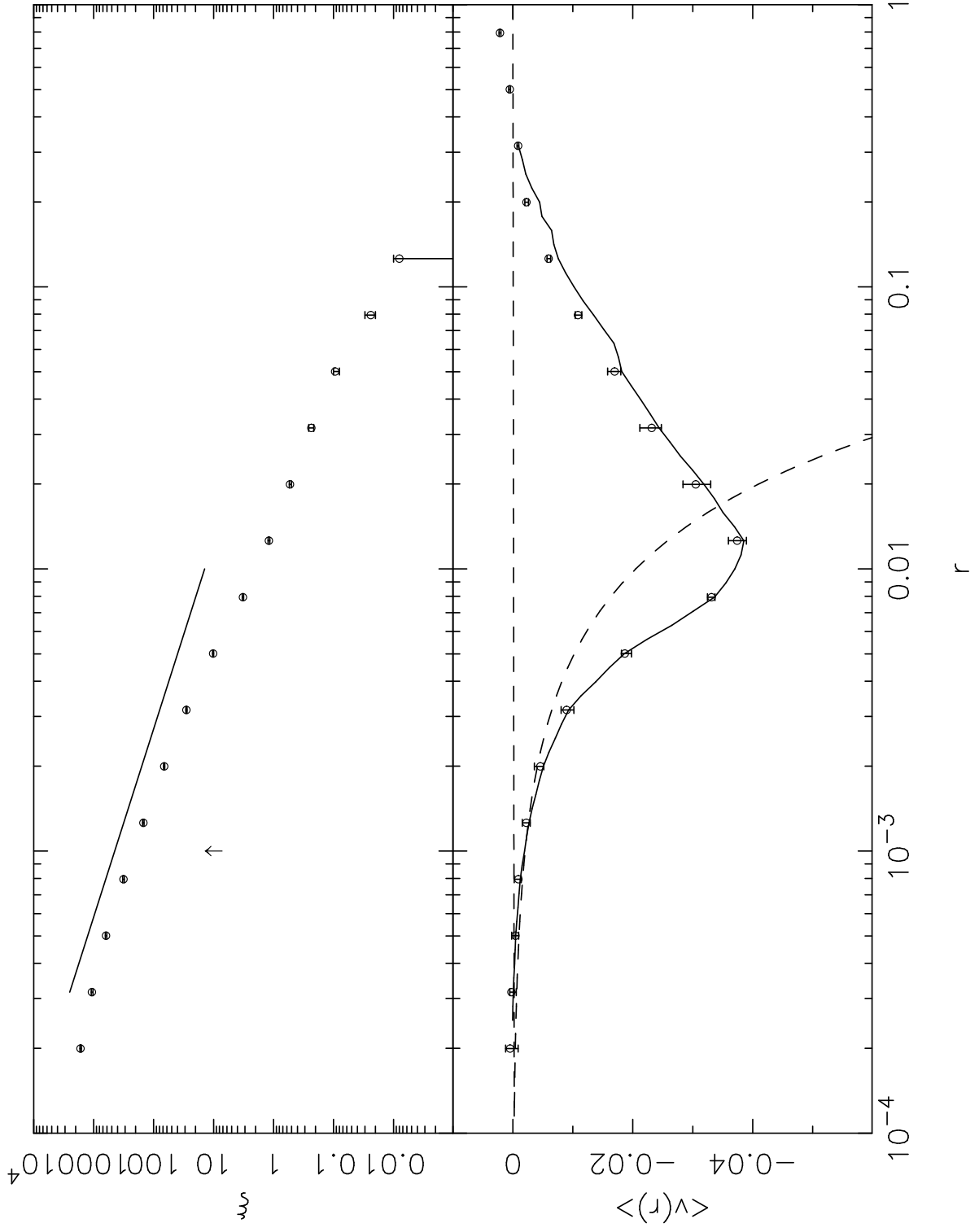


Fig. 4

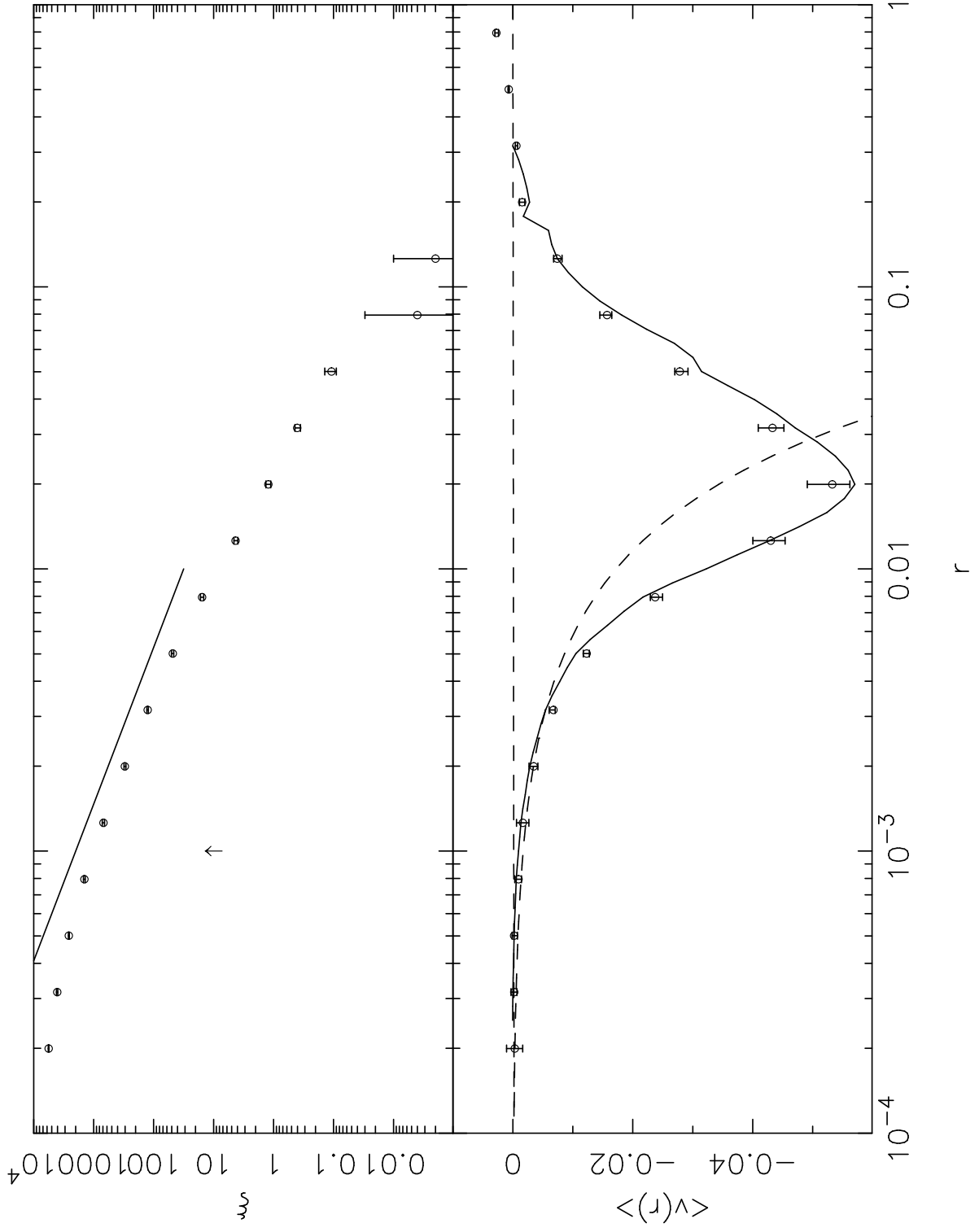


Fig. 5

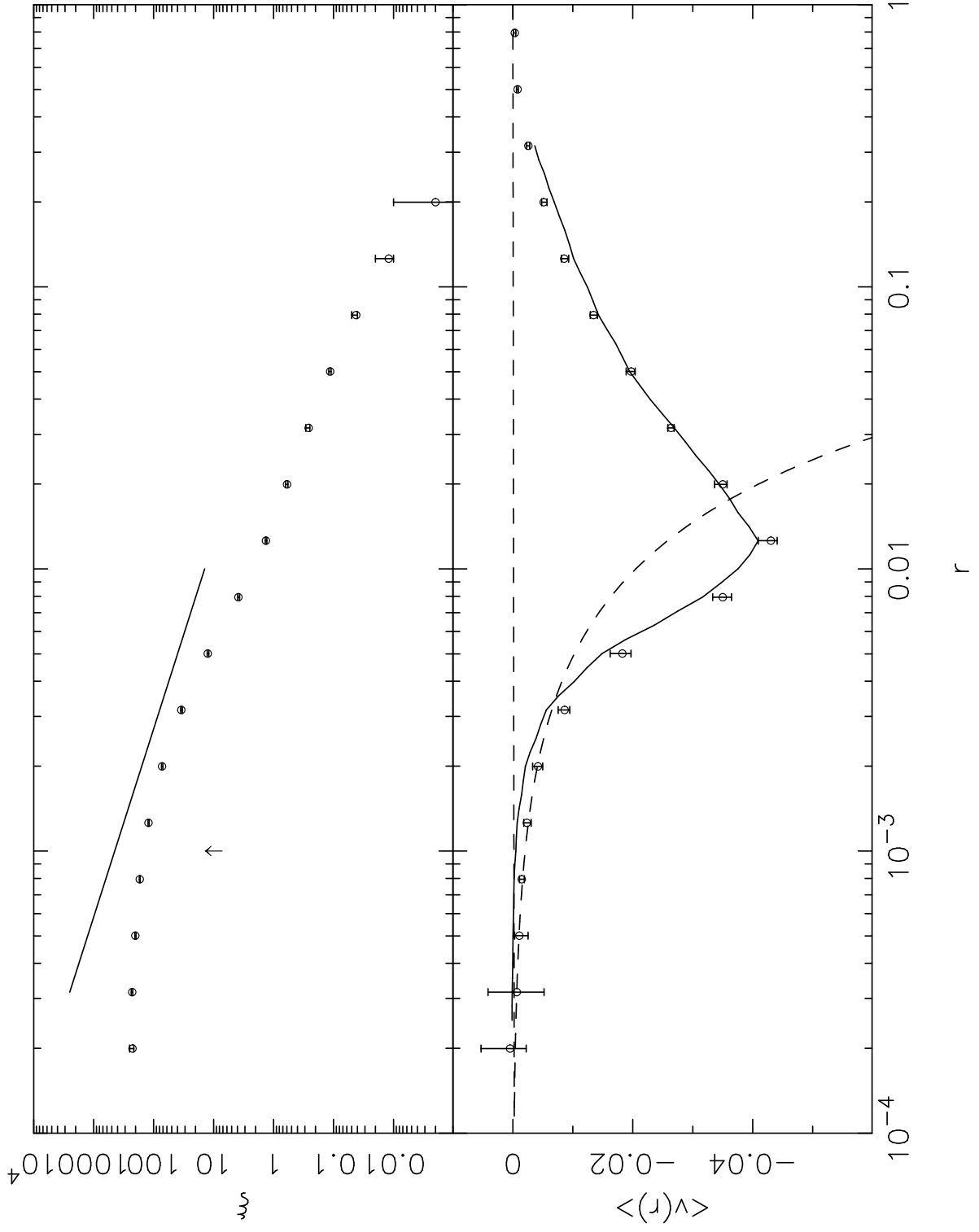


Fig. 6

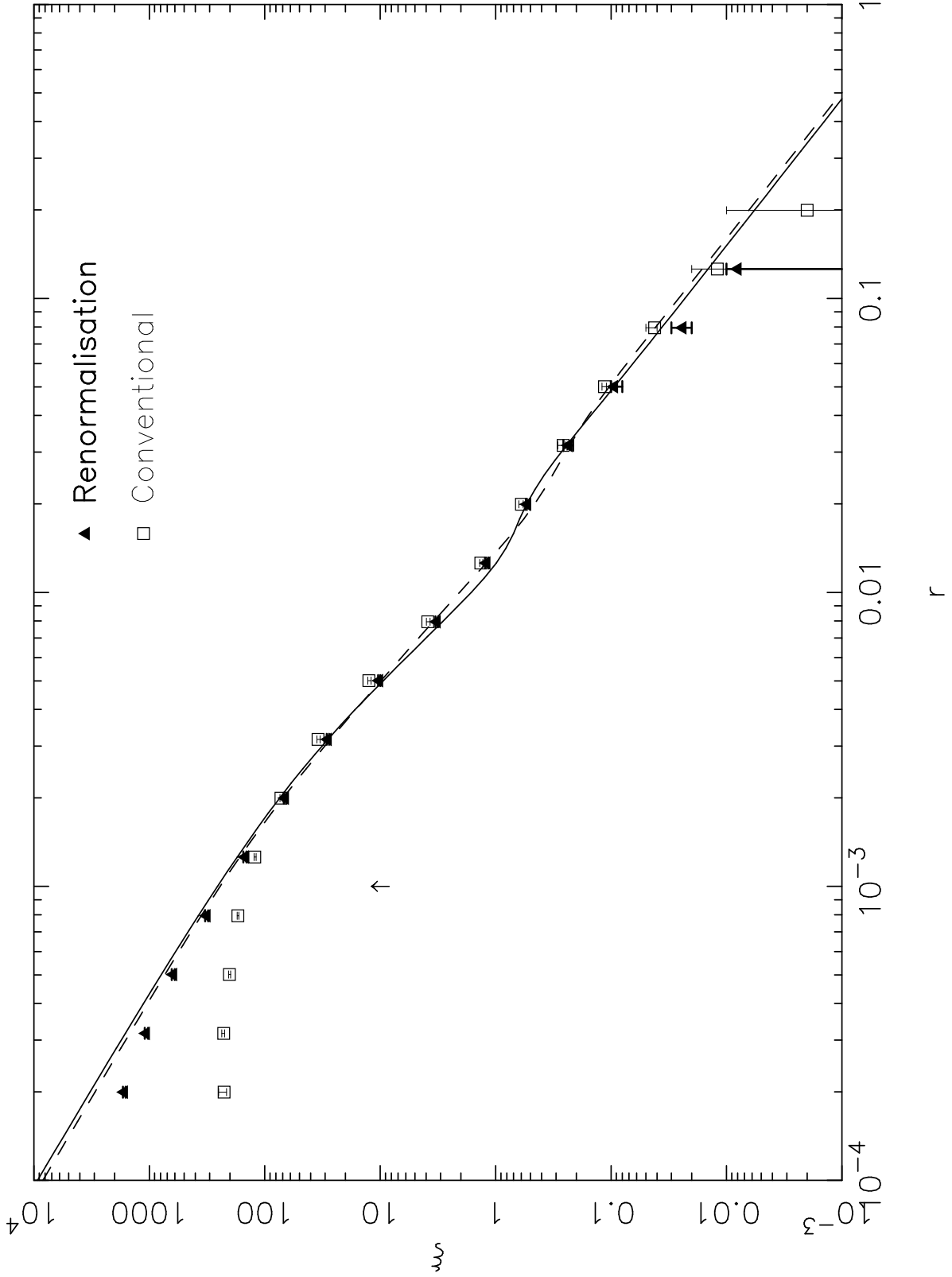


Fig. 7

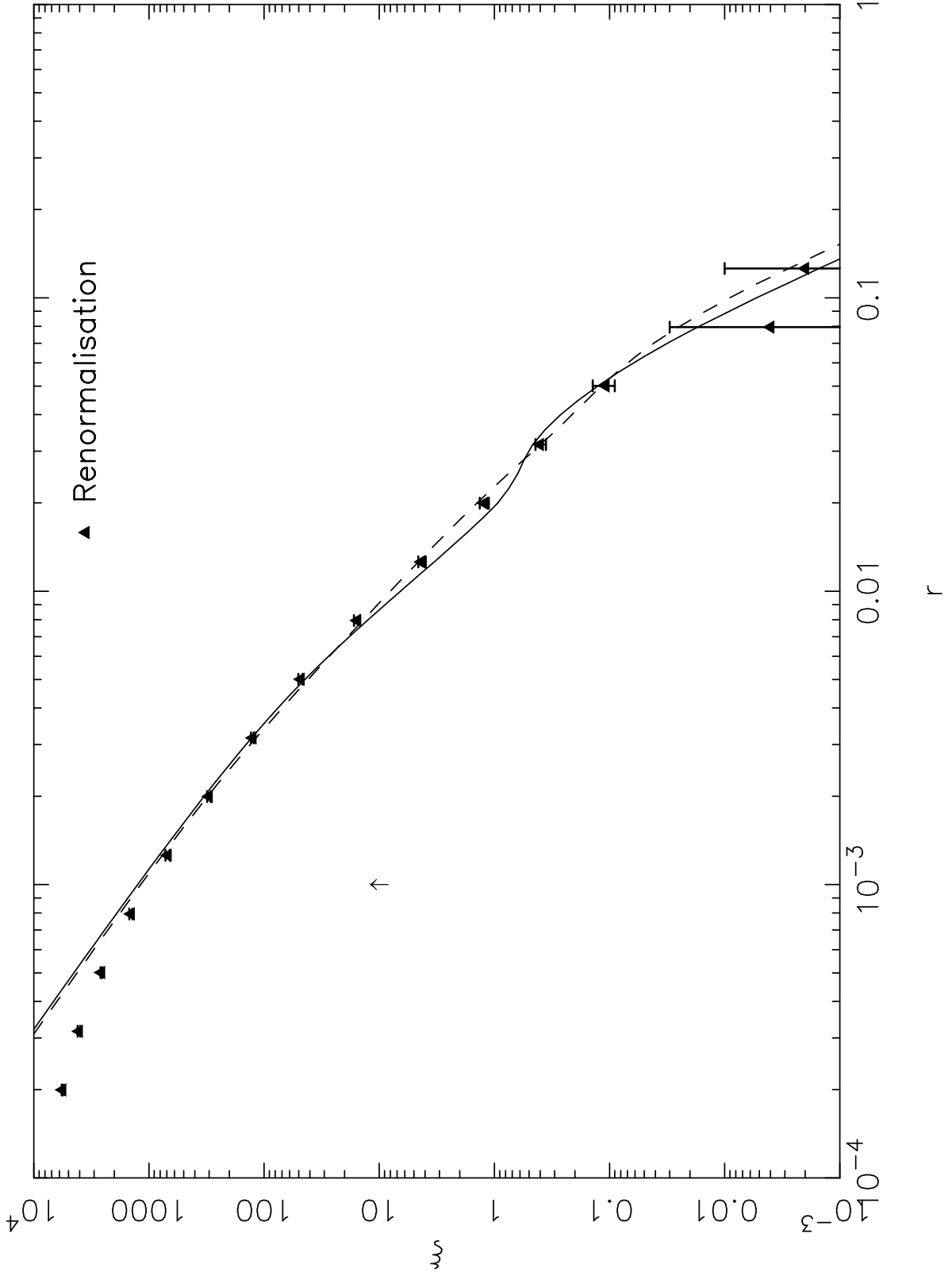


Fig. 8

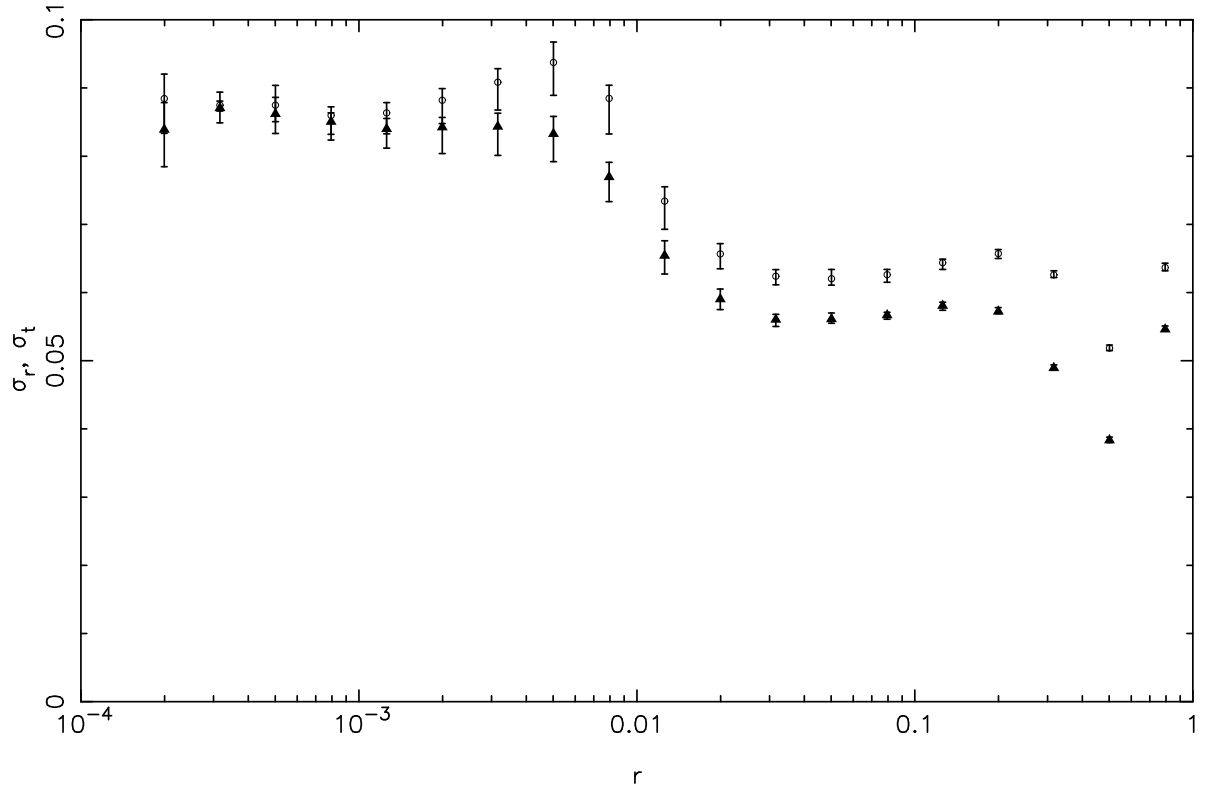
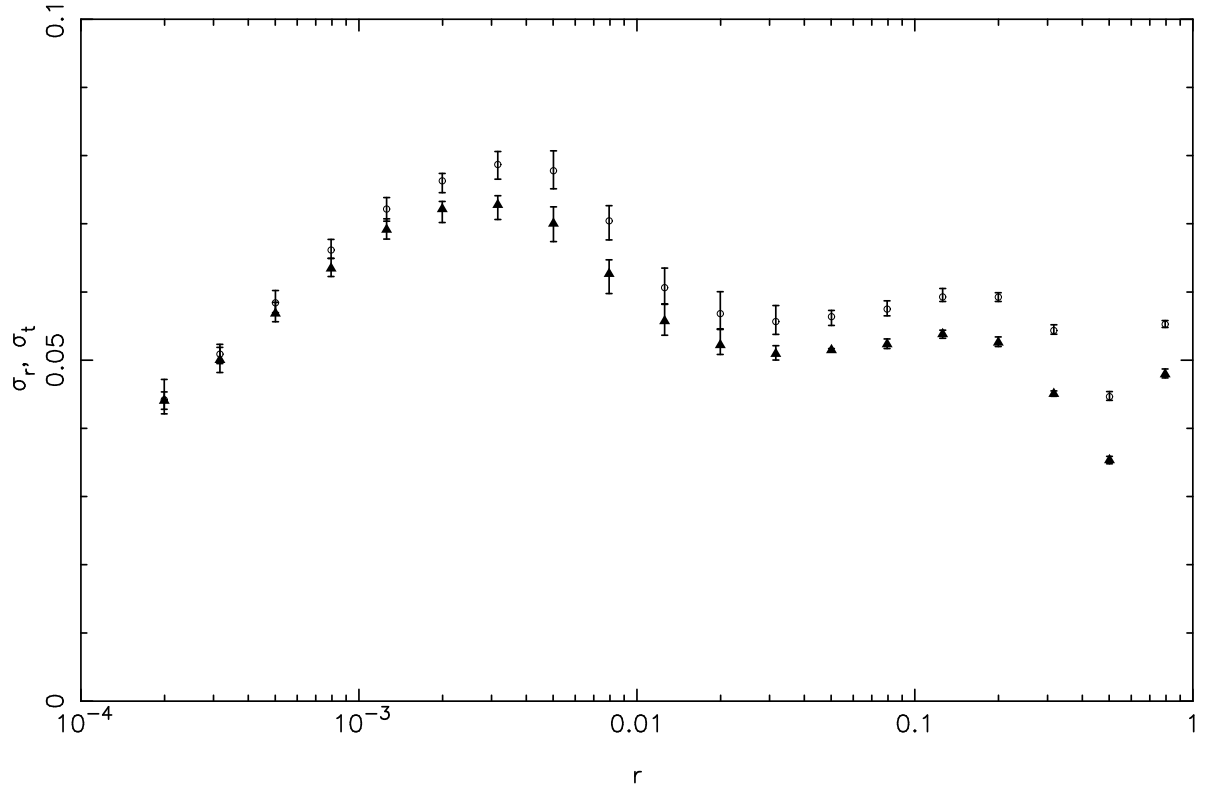


Fig. 9

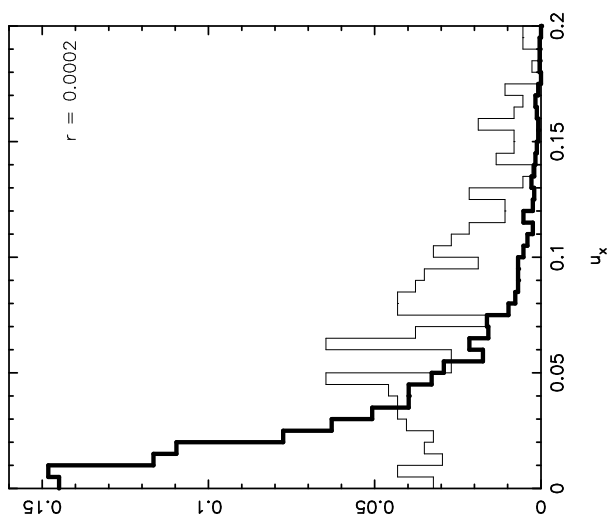
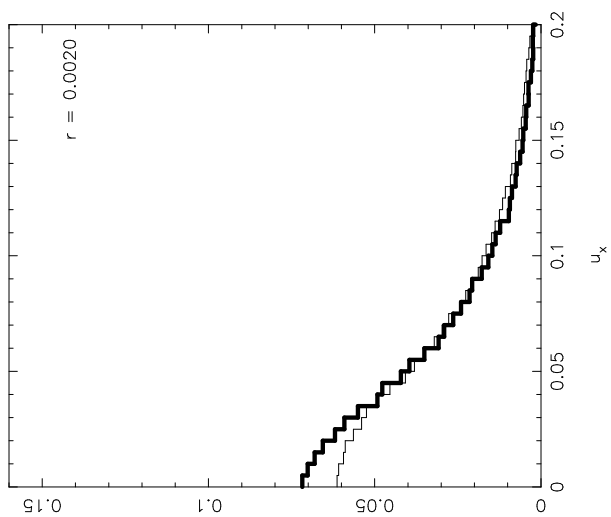
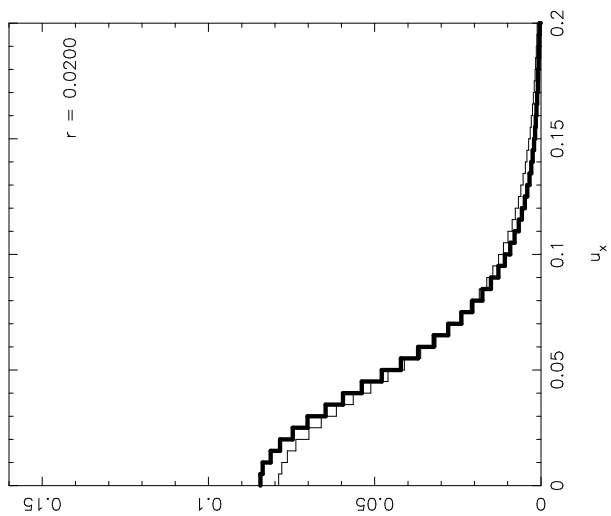


Fig. 10

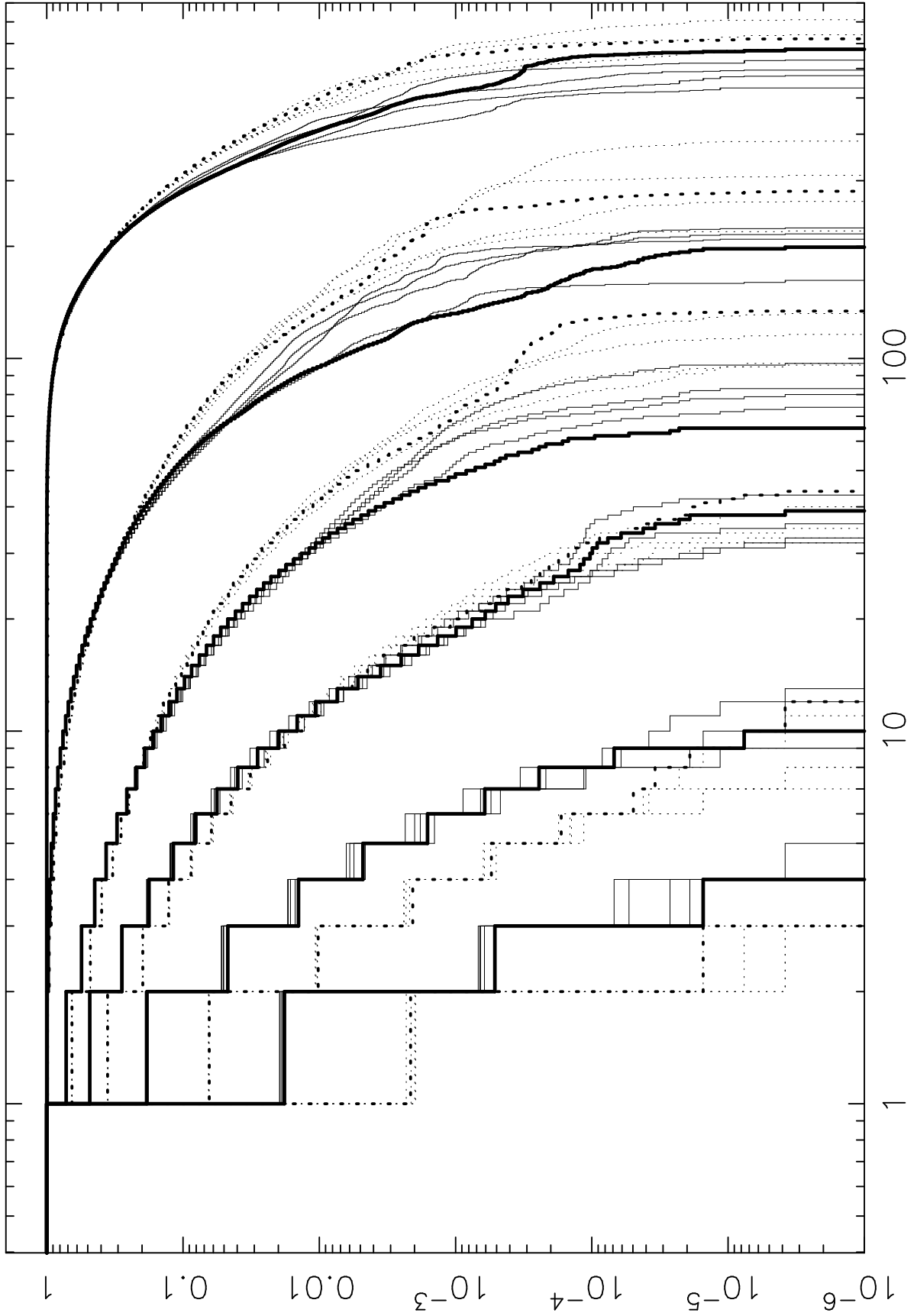


Fig. 11

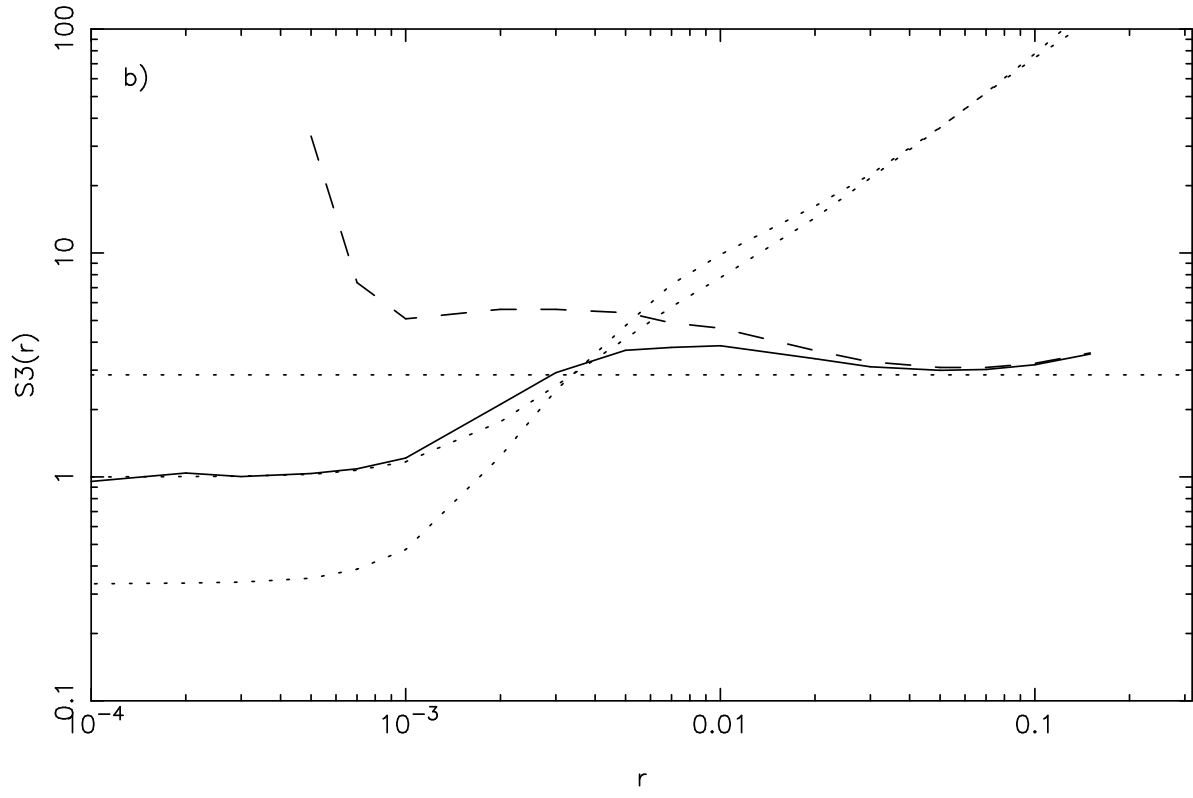
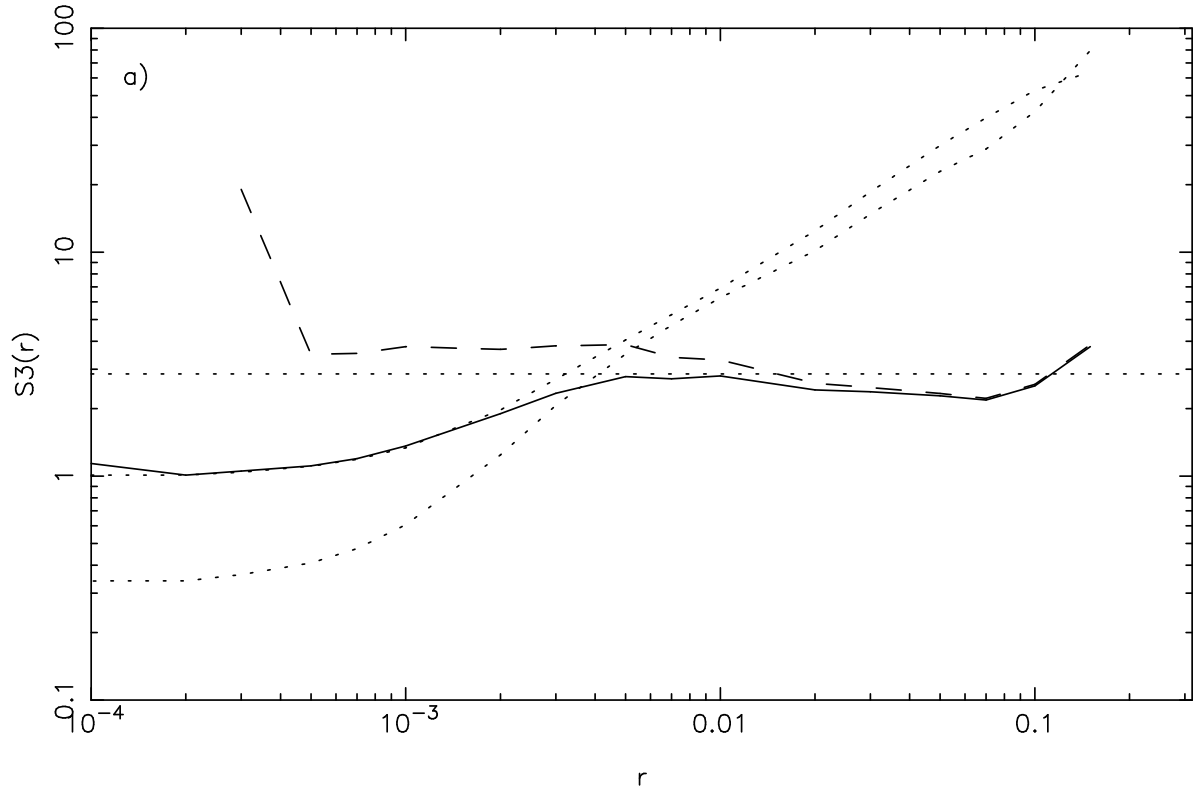


Fig. 12